

Embed Any NeRF: Graph Meta-Networks for Neural Tasks on Arbitrary NeRF Architectures

Francesco Ballerini¹ Pierluigi Zama Ramirez¹ Samuele Salti¹ Luigi Di Stefano¹

Abstract

Neural Radiance Fields (NeRFs) have emerged as a groundbreaking paradigm for representing 3D objects and scenes by encoding shape and appearance information into the weights of a neural network. Recent works have shown how such weights can be used as input to frameworks processing them to solve deep learning tasks. Yet, these frameworks can only process NeRFs with a specific, predefined architecture. In this paper, we present the first framework that can ingest NeRFs with multiple architectures and perform inference on architectures unseen at training time. We achieve this goal by training a Graph Meta-Network in a representation learning framework. Moreover, we show how a contrastive objective is conducive to obtaining an architecture-agnostic latent space. In experiments on both MLP-based and tri-planar NeRFs, our approach demonstrates robust performance in classification and retrieval tasks that either matches or exceeds that of existing frameworks constrained to single architectures, thus providing the first architecture-agnostic method to perform tasks on NeRFs by processing their weights.

1. Introduction

Neural Radiance Fields (NeRFs) (Mildenhall et al., 2020) have emerged over the last few years as a new paradigm for representing 3D objects and scenes (Xie et al., 2022). A NeRF is a neural network trained on a collection of images to map 3D coordinates to color and density values, which can then be used to synthesize novel views of the underlying object or scene via volume rendering. Due to their continuous nature, NeRFs can encode an arbitrary number of images at any resolution into a finite number of neural network weights, thus decoupling the number of

¹University of Bologna, Italy. Correspondence to: Francesco Ballerini <francesco.ballerini4@unibo.it>.

Preprint. Under review.

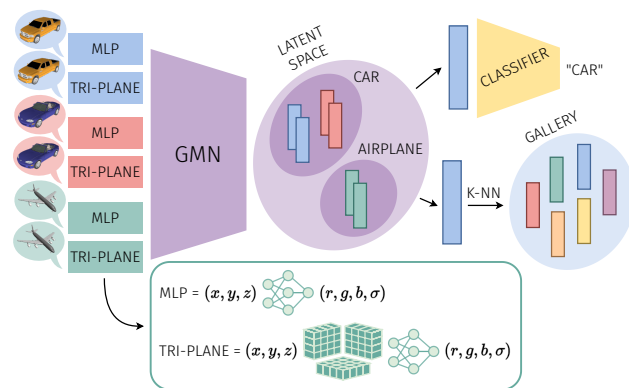


Figure 1. Framework overview. Our representation learning framework leverages a Graph Meta-Network (Lim et al., 2024) encoder to map weights of NeRFs with different architectures to a latent space where NeRFs representing similar objects are close to each other, independently of their architecture. The resulting embeddings are then used as input to downstream pipelines for either classification or retrieval tasks.

observations and their spatial resolution from the memory required to store the 3D representation. As a result, NeRFs hold the potential to become a standard tool for storing and communicating 3D information, as supported by the recent publication of several NeRF datasets (De Luigi et al., 2023; Hu et al., 2023; Zama Ramirez et al., 2024; Cardace et al., 2024).

With the rise of NeRFs as a new data format, whether and how it is possible to perform traditional deep-learning tasks on them has become an increasingly relevant research question. The naive solution to this problem involves rendering views of the underlying object from its NeRF representation and leveraging existing neural architectures designed to process images. However, this procedure requires additional computation time and several decisions that are likely to impact its outcome, such as the number of views to render, their viewpoint, and their resolution. A more elegant and efficient approach explored by recent works relies instead on performing tasks on NeRFs by processing their weights as input, therefore requiring no rendering step. This strategy is adopted by `nf2vec` (Zama Ramirez et al., 2024), a representation learning framework that learns to map MLP

NeRF weights to latent vectors by minimizing a rendering loss. These vectors are then used as input to standard deep-learning pipelines for downstream tasks. A related approach is proposed by [Cardace et al., 2024](#), who, instead of employing traditional MLPs, leverage tri-planar NeRF representations ([Chan et al., 2022](#)), where input coordinates are projected onto three orthogonal planes of learnable features to compute the input for an MLP.

Both `nf2vec` and the method by [Cardace et al.](#), however, perform tasks with neural frameworks designed to ingest a specific type of NeRF architecture (i.e. MLPs with predefined hidden dimensions in `nf2vec` and tri-planes with set spatial resolution in [Cardace et al.](#)), which makes them unable to process arbitrary input architectures. In the context of a research domain where new NeRF designs are constantly being explored ([Xie et al., 2022](#)), this limitation strongly hinders their applicability. The issue of handling arbitrary input architectures has recently been studied in the broader research field on *meta-networks*, i.e. neural networks that process other neural networks as input. Specifically, Graph Meta-Networks (GMNs) have been proposed ([Lim et al., 2024](#); [Kofinas et al., 2024](#)), namely Graph Neural Networks (GNNs) that can ingest any neural architecture as long as it can be first converted into a graph. Yet, these works do not experiment with NeRFs as input to their GMNs.

Motivated by the potential of GMNs to process diverse NeRF architectural designs, we investigate whether a GMN encoder can learn a latent space where distances reflect the similarity between the actual content of the radiance fields rather than their specific neural parameterization. Our empirical study reveals that this latent space organization cannot be achieved by solely relying on a rendering loss ([Zama Ramirez et al., 2024](#)), as such loss alone causes different NeRF architectures to aggregate into distinct clusters in the embedding space, even when they represent the same underlying object. To overcome this limitation, we draw inspiration from the contrastive learning literature and introduce a SigLIP loss term ([Zhai et al., 2023](#)) that places pairs of NeRFs with different architectures representing the same object closer to each other in latent space while pushing other pairs further apart. Combined with a rendering loss, this approach produces an architecture-agnostic embedding space organized by class and instance. We then show that our encoder produces latent representations that serve as effective inputs for downstream tasks such as classification and retrieval. [Figure 1](#) outlines our framework key components when NeRF architectures are MLP ([Zama Ramirez et al., 2024](#)) and tri-plane ([Cardace et al., 2024](#)).

Our contributions can be summarized as follows:

- To the best of our knowledge, we are the first to perform tasks on NeRFs by processing their weights with an approach that is agnostic to their architecture;

- Our framework is also the first that can handle NeRF architectures unseen at training time;
- By means of a contrastive learning objective, we enforce a latent space where NeRFs with similar content are close to each other, regardless of their architecture;
- Our method can seamlessly handle arbitrary NeRF architectures while achieving comparable or superior results to previous methods operating on single architectures.

2. Related Work

Neural Radiance Fields. NeRFs were first introduced by [Mildenhall et al., 2020](#) as a method for novel view synthesis, namely the task of generating previously unseen views of a scene from a set of sparse input images taken from different viewpoints. In the original formulation, a NeRF is an MLP that parameterizes a function $(x, y, z, \theta, \phi) \mapsto (r, g, b, \sigma)$ that maps a 3D position (x, y, z) and a 2D viewing direction (θ, ϕ) to an emitted color (r, g, b) and volume density σ . Since then, several architectural variants have been proposed, many of which combine the MLP with a trainable discrete data structure that quantizes the space of input coordinates and maps them to a higher-dimensional vector, which becomes the actual MLP input. These structures, which include voxel grids ([Liu et al., 2020](#)), tri-planes ([Chan et al., 2022](#)), and hash tables ([Müller et al., 2022](#); [Barron et al., 2023](#)), typically result in NeRF architectures that can be trained much faster to convergence without sacrificing rendering quality. Our work focuses on the NeRF architectures proposed by [Zama Ramirez et al., 2024](#) and [Cardace et al., 2024](#), consisting of a single MLP and a tri-plane followed by an MLP, respectively. In both cases, the MLP adheres to the simplified formulation by [Mildenhall et al., 2020](#) with no viewing direction, i.e. $(x, y, z) \mapsto (r, g, b, \sigma)$.

Meta-networks. Due to the high dimensionality of the weight space, its symmetries ([Hecht-Nielsen, 1990](#)), and the impact of randomness on the solution where training converges ([Entezari et al., 2022](#); [Ainsworth et al., 2023](#)), processing neural network weights presents unique challenges that set them apart from more common input formats. The first works to address the design of neural networks that ingest the weights of other neural networks leverage group theory to devise architectures that are equivariant to the permutation symmetries of the input networks ([Navon et al., 2023](#); [Zhou et al., 2023a;b](#)). Yet, these meta-networks are tailored to specific input networks, such as MLPs and CNNs without normalization layers, and cannot generalize to arbitrary input architectures. To overcome this limitation, Graph Meta-Networks (GMNs) were introduced ([Lim et al., 2024](#); [Kofinas et al., 2024](#)). Since GMNs are graph neural networks, they are, by design, equivariant to the node permutations of input graphs and can ingest any type of graph. Therefore, the challenge of processing neural net-

work weights turns into the task of transforming the input network into a graph. This process is straightforward for an MLP, as it is sufficient to consider its computation graph; for other architectures, however, different strategies are necessary to prevent an exponential growth in the number of edges, especially when weight sharing occurs. In this paper, we borrow the GMN formulation by Lim et al., 2024 as well as their method for converting networks into graphs.

Meta-networks for NeRF processing. Being the meta-network literature still in its infancy, none of the aforementioned works include NeRFs as input in their experimental evaluation and choose instead to focus on simpler neural networks. The first methods to perform tasks on NeRFs by ingesting their weights are `nf2vec` (Zama Ramirez et al., 2024) and the framework by Cardace et al., 2024. `nf2vec` is an encoder-decoder architecture trained end-to-end with a rendering loss; at inference time, the encoder takes the weights of a NeRF as input and produces an embedding which in turn becomes the input to traditional deep-learning pipelines for downstream tasks. More recent works (Ballerini et al., 2024; Amaduzzi et al., 2024) investigate the potential applications of this approach to language-related tasks. While `nf2vec` is designed to ingest MLPs, Cardace et al. leverage an existing NeRF architecture consisting of a tri-plane followed by a smaller MLP (Chan et al., 2022), which enables them to perform tasks on NeRFs by discarding the MLP and processing the tri-planar component alone with a Transformer. Yet, both `nf2vec` and Cardace et al. suffer from the same drawback as the first meta-networks: they are designed to handle specific NeRF architectures. Therefore, the idea behind our work is to combine the architecture-agnostic GMNs with the representation learning framework proposed by Zama Ramirez et al. to obtain a method that can perform tasks on NeRFs via their weights independently of the underlying architecture.

Contrastive learning. Contrastive learning is a representation learning approach that trains models to distinguish between similar (positive) and dissimilar (negative) data pairs by aiming to embed similar data points closer together while pushing dissimilar ones farther apart in latent space. In self-supervised contexts, contrastive learning generates positive pairs through data augmentations of the same instance and treats other instances as negatives, enabling models to learn augmentation-invariant and task-agnostic features without relying on labeled data, as exemplified by SimCLR (Chen et al., 2020) and MoCo (He et al., 2020). Multimodal vision-language models extend this concept to align image and text modalities by maximizing the similarity between matching image-text pairs and minimizing it for mismatched ones, as demonstrated in CLIP (Radford et al., 2021), a model that learns a shared embedding space supporting zero-shot transfer to diverse vision tasks. Zhai et al., 2023 build upon this foundation and propose to replace the softmax-based loss

used in CLIP with a simple pairwise sigmoid loss, called SigLIP, which is shown to work better for relatively small (4k–32k) batch sizes. In this paper, we use the SigLIP loss to align GMN embeddings of different NeRF architectures representing the same object.

3. Method

We tackle the challenging problem of embedding NeRFs parameterized by different neural architectures with a representation learning framework consisting of an encoder and a decoder trained end-to-end with a combination of rendering and contrastive objectives, where the encoder is implemented by a Graph Meta-Network (GMN). After training, the frozen encoder converts NeRF weights into an embedding that can serve as input to standard deep-learning pipelines for downstream tasks. In the remainder of this section, we will detail each framework component. Further details are provided in Appendix B.

From NeRFs to graphs. In order for a NeRF to be ingested by the encoder, it must be first converted into a graph. The naive approach to perform this conversion would be to adopt the standard computation graph formulation, namely representing a neural network as a Directed Acyclic Graph (DAG) where nodes are activations and edges hold weight values. However, computation graphs scale poorly with the number of activations in networks with weight-sharing schemes, as a single weight requires multiple edges, one for each activation it affects. This limitation has motivated Lim et al., 2024 to introduce the *parameter graph* representation, where each weight is associated with a single edge of the graph instead of multiple edges. Furthermore, differently from computation graphs, parameter graphs may include additional node and edge features that increase the expressive power of the meta-networks processing them, such as layer index, node index within a layer, node or edge type (e.g. either weight or bias), and position within a kernel or grid. Lim et al. 2024 describe the parameter graph construction of several common neural layers, including spatial parameter grids such as those used in many NeRF architectures (Liu et al., 2020; Chan et al., 2022; Müller et al., 2022). These per-layer subgraphs can then be concatenated to form the overall parameter graph. In this paper, we are specifically interested in graph representations of MLPs (hence, linear layers) and tri-planes (Chan et al., 2022). The parameter subgraph of a linear layer coincides with its computation graph, except for biases, which are modeled by including an additional node for each layer, connected to every other neuron in the layer with an edge containing the bias value. Grids like those used in tri-planes are instead modeled by one node for each spatial location and one node for each feature channel, where each spatial node is connected via an edge to every channel node; the channel nodes, together

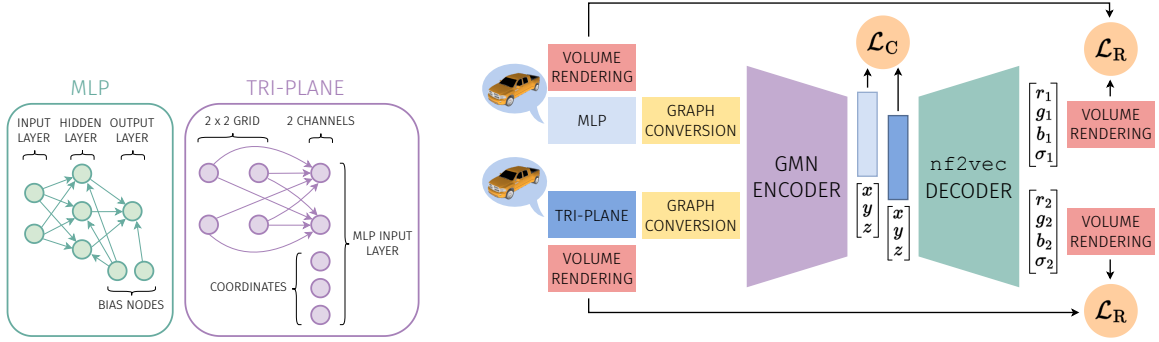


Figure 2. **Method overview.** **Left:** parameter graph construction (Lim et al., 2024) for an MLP (left) and a tri-plane (right). For simplicity, only the graph of a single plane is shown. **Right:** our framework leverages Graph Meta-Networks (Lim et al., 2024) as encoders and the `nf2vec` decoder (Zama Ramirez et al., 2024), trained end-to-end with both a rendering (\mathcal{L}_R) and a contrastive (\mathcal{L}_C) loss on a dataset of NeRFs with different architectures (MLPs and tri-planes).

with one node for each input coordinate, become the first layer of the MLP parameter graph that follows. An example of graph construction for an MLP and a tri-planar grid is shown in Figure 2 (left). Our framework leverages the parameter graph representation by converting input NeRFs to parameter graphs before feeding them to the encoder.

Encoder. Our framework’s encoder is the GMN proposed by Lim et al., 2024, i.e. a standard message-passing Graph Neural Network (GNN) (Battaglia et al., 2018) with node and edge features but no global graph-level feature. Node features are updated by message-passing along neighbors and contribute to updating the features of the edges connecting them. The final embedding is obtained via an average pooling of the edge features. Notably, as the encoder is a GNN, it can process any input graph and, hence, any neural network that has undergone the previously described parameter-graph conversion, thereby allowing our framework to handle any NeRF architecture for which a graph representation is known.

Decoder. Our framework leverages the decoder first introduced by `nf2vec` (Zama Ramirez et al., 2024), which takes as input the concatenation of the embedding produced by the encoder alongside a frequency encoding (Mildenhall et al., 2020) of a 3D point (x, y, z) and outputs a learned approximation of the radiance field value (r, g, b, σ) at that point. Thus, the combination of decoder and embedding can itself be seen as a conditioned neural radiance field. Inspired by Park et al., 2019, the decoder architecture is a simple succession of linear layers intertwined with ReLU activations and a single skip connection from the input to halfway through the network.

Training. The encoder and the decoder are trained end-to-end with a combination of two loss terms, which, from now on, will be referred to as *rendering loss* and *contrastive loss*. The rendering loss is the one used by Zama Ramirez

et al., 2024 to train the `nf2vec` framework and can be described as follows. Consider a NeRF $\mathcal{N}: \mathbf{x} \mapsto (\mathbf{c}, \sigma)$ with $\mathbf{x} = (x, y, z)$ and $\mathbf{c} = (r, g, b)$ and let $I \in \mathcal{I}$ be one of the images \mathcal{N} was trained on, with corresponding camera pose and intrinsic parameters. Let $\mathcal{X} = \{\mathbf{x}_i\}$ be the set of points sampled along a ray cast from camera I into the scene and passing through pixel \mathbf{p} on the image plane, and let $C_{\mathcal{N}}(\mathbf{p})$ be the color computed via volume rendering by accumulating the contributions of the (\mathbf{c}_i, σ_i) output values of \mathcal{N} for all inputs $\mathbf{x}_i \in \mathcal{X}$. Analogously, let $C_{\mathcal{D}}(\mathbf{p})$ be the color computed with the output values produced by the decoder when the encoder takes \mathcal{N} as input. The rendering loss associated with NeRF \mathcal{N} is then defined as

$$\mathcal{L}_R(\mathcal{N}) = \sum_{I \in \mathcal{I}} \sum_{\mathbf{p} \in S(I)} \text{smoothL1}(C_{\mathcal{N}}(\mathbf{p}), C_{\mathcal{D}}(\mathbf{p})) \quad (1)$$

where $S(I)$ is a subset of pixels sampled from \mathcal{I} and `smoothL1` is the smooth L1 loss (Girshick, 2015). More precisely, Zama Ramirez et al. compute one rendering loss term for foreground and one for background pixels and express \mathcal{L}_R as a weighted sum of the two. Let \mathcal{M} and \mathcal{T} be two NeRF architectures, e.g. MLP-based (Zama Ramirez et al., 2024) and tri-planar (Cardace et al., 2024), respectively, and consider a dataset of NeRFs of 3D objects where each object j appears twice, once as \mathcal{M}_j and then as \mathcal{T}_j . Given a mini-batch $\mathcal{B} = \{(\mathcal{M}_1, \mathcal{T}_1), (\mathcal{M}_2, \mathcal{T}_2), \dots\}$, the rendering loss of \mathcal{B} is the average rendering loss of each NeRF in \mathcal{B} , i.e.

$$\mathcal{L}_R = \frac{1}{2|\mathcal{B}|} \sum_j \sum_{\mathcal{N} \in (\mathcal{M}_j, \mathcal{T}_j)} \mathcal{L}_R(\mathcal{N}) \quad (2)$$

where $\mathcal{L}_R(\mathcal{N})$ is the one defined in Equation (1). Our contrastive loss follows instead the definition by Zhai et al., 2023, namely

$$\mathcal{L}_C = -\frac{1}{|\mathcal{B}|} \sum_{j=1}^{|\mathcal{B}|} \sum_{k=1}^{|\mathcal{B}|} \ln \frac{1}{1 + e^{-\ell_{jk}(t\mathbf{u}_j \cdot \mathbf{v}_k + b)}} \quad (3)$$

where $\ell_{jk} = 1$ if $j = k$ and -1 otherwise, t and b are learnable scalar hyper-parameters, and \mathbf{u}_j and \mathbf{v}_k are L2-normalized encoder embeddings of \mathcal{M}_j and \mathcal{T}_k , respectively. Finally, the combined loss is

$$\mathcal{L}_{R+C} = \mathcal{L}_R + \lambda \mathcal{L}_C, \quad (4)$$

where λ is a fixed hyper-parameter. Figure 2 (right) shows an overview of our training procedure. The purpose of the rendering loss \mathcal{L}_R is to guide the encoder in learning embeddings that, rather than encoding the input NeRF weights, capture meaningful information about the appearance of the 3D object represented by those weights; this is achieved by promoting decoder output values that lead to rendered object views that closely resemble those rendered from the NeRF itself. Therefore, \mathcal{L}_R enforces a latent space where NeRFs representing similarly shaped and/or colored objects (e.g. those belonging to the same class) are closer than those that differ in appearance. However, \mathcal{L}_R by itself is not able to capture the notion that different NeRF architectures representing the same object provide equivalent parameterizations of the same underlying radiance field and should thus be mapped to the same point in latent space. Instead, for any given class, \mathcal{L}_R creates distinct clusters associated with different architectures, as shown in Figure 3 (left). To overcome this limitation and encourage the creation of an embedding space organized according to the content of the underlying signal rather than its neural network parameterization, we introduce the contrastive loss \mathcal{L}_C , which leverages the availability at training time of NeRFs of the same object parameterized by different architectures to learn to treat them as alternative but equivalent representations of the same data point. Hence, the combination of \mathcal{L}_R and \mathcal{L}_C should result in a latent space where NeRFs of similar objects are close to each other, independently of their NeRF architecture; in other words, architectural differences should not lead to greater distances between embeddings, only differences in appearance should. This claim is experimentally validated in Figure 3 (middle) and further discussed in Section 4.1.

Inference. At inference time, a single forward pass of the encoder converts the parameter graph of a NeRF into a latent vector, which we then use as input to standard deep-learning pipelines for classification and retrieval tasks, as outlined in Figure 1 and detailed in Sections 4.2 and 4.3.

4. Experiments

Dataset. All our experiments are performed on two datasets of NeRFs: the one by Zama Ramirez et al., 2024 and the one by Cardace et al., 2024. They both consist of NeRFs trained on ShapenetRender (Xu et al., 2019), a dataset providing RGB images of synthetic 3D objects together with their class label. The difference between these two datasets lies in the

NeRF architecture used to create them: in Zama Ramirez et al., a NeRF is an MLP, whereas in Cardace et al. is a tri-plane followed by an MLP. Both Zama Ramirez et al.’s and Cardace et al.’s MLPs have 3 hidden layers with dimension 64, and Cardace et al.’s tri-planes have spatial resolution 32×32 and 16 channels. Our experimental evaluation is based on three alternative training sets: (i) One consisting of Zama Ramirez et al.’s MLP-based NeRFs only, which will be referred to as MLP; (ii) One consisting of Cardace et al.’s tri-planar NeRFs only, which will be referred to as TRI; (iii) The union of Zama Ramirez et al.’s and Cardace et al.’s datasets, i.e. a dataset where each ShapenetRender object appears twice, once as an MLP-based and then as a tri-planar NeRF, which will be referred to as BOTH.

Models. In order to assess the impact of the different losses on training, we introduce a distinction between three versions of our framework, depending on the learning objective: (i) \mathcal{L}_R , where the framework has been trained only with the rendering loss of Equation (2); (ii) \mathcal{L}_{R+C} , where the framework has been trained with a combination of rendering and contrastive losses as in Equation (4). We set $\lambda = 2e-2$, as it leads to similar magnitudes in the two terms; (iii) \mathcal{L}_C , where the framework has been trained only with the contrastive loss of Equation (3).

Single vs multi-architecture. Our method is the first neural processing framework able to handle multiple NeRF architectures. Thus, the natural setting to test it is when it is trained on BOTH; we will refer to this scenario as the *multi-architecture setting*. Yet, our method can also be used when the input NeRFs all share the same architecture, e.g. when our framework has been trained on either the MLP or the TRI dataset only, by dropping the contrastive loss. Therefore, to test its generality, we perform experiments in such a scenario, which we will refer to as the *single-architecture setting*. In this setting, our approach can be compared against previous methods (Zama Ramirez et al.; Cardace et al.) that can only handle specific architectures.

4.1. Latent Space Analysis

To study the impact of different learning objectives on the organization of the resulting NeRF latent space, we apply the t-SNE dimensionality reduction (Van der Maaten & Hinton, 2008) to the embeddings computed by our framework on NeRFs belonging to the test set of the BOTH dataset. Figure 3 shows the resulting bi-dimensional plots. Some interesting patterns can be noted. When trained to minimize \mathcal{L}_R alone (Figure 3, left), the encoder creates an embedding space that is clustered by class, even if class labels have not been used at training time. This behavior is a byproduct of the loss, which enforces NeRFs encoding similar shapes and colors to be nearby in the latent space. Another byproduct one could expect is that the same object under different

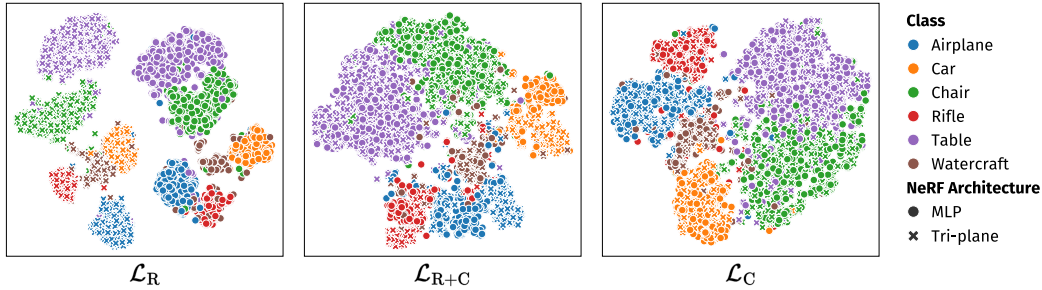


Figure 3. **t-SNE plots.** 2D projections of the latent space created by the GMN encoder when trained on a dataset of both MLP-based and tri-planar NeRFs of ShapenetRender objects (Xu et al., 2019). Only test-set embeddings are shown.

Method	Classifier Training Set	Accuracy (%) \uparrow		
		BOTH	MLP	TRI
<i>nf2vec</i>		—	—	—
Cardace et al.		—	—	—
\mathcal{L}_R (ours)	BOTH	93.5	93.5	93.5
\mathcal{L}_{R+C} (ours)		91.9	91.8	91.9
\mathcal{L}_C (ours)		86.2	87.3	85.1
<i>nf2vec</i>		—	—	—
Cardace et al.		—	—	—
\mathcal{L}_R (ours)	MLP	49.9	93.6	6.2
\mathcal{L}_{R+C} (ours)		82.1	92.4	71.9
\mathcal{L}_C (ours)		80.6	87.5	73.6
<i>nf2vec</i>		—	—	—
Cardace et al.		—	—	—
\mathcal{L}_R (ours)	TRI	64.5	35.5	93.4
\mathcal{L}_{R+C} (ours)		81.1	70.1	92.1
\mathcal{L}_C (ours)		83.7	82.4	85.1

Table 1. **NeRF classification (multi-architecture).** The encoder is trained on BOTH; the classifier is trained on the datasets in column 2 and tested on those in columns 3–5.

NeRF architectures is projected into the same embedding, since the decoder output, and therefore the condition computed by the encoder, has to be the same for both NeRFs. However, this turns out not to be the case. Instead, two distinct clusters emerge for each class, each corresponding to a NeRF architecture, and these clusters are further away from each other than clusters sharing the same underlying architecture. This outcome shows that \mathcal{L}_R alone does not directly encourage the model to align NeRF embeddings regardless of the input architecture. Conversely, when trained to minimize \mathcal{L}_C alone (Figure 3, right), the encoder creates a single cluster per class, causing input architectures to be indistinguishable in the plot. However, gaps between classes reduce, especially for objects with similar shapes and colors, like *chairs* and *tables* or *airplanes* and *watercrafts*. \mathcal{L}_{R+C} (Figure 3, middle) strikes a balance between these latent space properties. Compared to \mathcal{L}_R , one macro-cluster per class is present, although for some classes, like *airplane* or *car*, it splits into sub-clusters according to the NeRF architecture. In other words, the latent space represents more the content than the architectures of the NeRFs, but it is not completely architecture-agnostic as when minimizing

Method	Encoder Training Set	Accuracy (%) \uparrow
<i>nf2vec</i>		92.1
Cardace et al.	MLP	—
\mathcal{L}_R (ours)		93.6
<i>nf2vec</i>		—
Cardace et al.	TRI	93.1
\mathcal{L}_R (ours)		94.0

Table 2. **NeRF classification (single-architecture).** The classifier is trained and tested on the same dataset the encoder is trained on.

\mathcal{L}_C alone. Compared to \mathcal{L}_C , classes are more separated, although not as much as with \mathcal{L}_R alone. Thus, we expect \mathcal{L}_R to be the best choice for tasks where the separation between classes is paramount; \mathcal{L}_C , on the other hand, is likely to be the most effective objective for tasks where strong invariance to the NeRF architecture is required; \mathcal{L}_{R+C} , finally, should provide good performance across all tasks.

4.2. NeRF Classification

Once our framework has been trained, NeRF classification is performed by learning a downstream classifier \mathcal{C} to predict the labels of the embeddings produced by the encoder; an overview of this procedure is outlined in Figure 1. Since the multi-architecture setting requires evaluating methods trained on BOTH, neither one of the previous works, i.e. *nf2vec* (Zama Ramirez et al., 2024) and Cardace et al., 2024, can be applied in this scenario, as they can be trained only on MLP and TRI, respectively. As a result, the only available methods for multi-architecture NeRF classification are the three variants of our framework, i.e. \mathcal{L}_R , \mathcal{L}_{R+C} , and \mathcal{L}_C . In the single-architecture setting, instead, previous methods can be trained and evaluated on the datasets corresponding to the NeRF architecture they can ingest, whereas neither \mathcal{L}_{R+C} nor \mathcal{L}_C can be applied, as there is a single architecture and, therefore, no positive pairs to compute the contrastive loss. Table 1 shows NeRF classification results in the multi-architecture setting. When \mathcal{C} has also been trained on BOTH, \mathcal{L}_R performs the best. This result is consistent with the better separation between the clusters corresponding to the different classes provided by \mathcal{L}_R , as

Method	Classifier Training Set	Accuracy (%) \uparrow					
		MLP-2L	MLP-32H	TRI-2L	TRI-32H	TRI-16W	TRI-8C
nf2vec		—	—	—	—	—	—
Cardace et al.		—	—	—	—	—	—
\mathcal{L}_R (ours)	BOTH	92.1	87.4	92.7	89.0	30.1	75.0
\mathcal{L}_{R+C} (ours)		87.4	85.8	90.3	86.4	63.7	21.3
\mathcal{L}_C (ours)		81.0	76.7	81.6	75.1	78.0	11.4
nf2vec		—	—	—	—	—	—
Cardace et al.		—	—	—	—	—	—
\mathcal{L}_R (ours)	MLP	91.1	83.3	6.1	9.8	4.6	7.3
\mathcal{L}_{R+C} (ours)		87.1	84.8	66.7	59.5	49.0	12.3
\mathcal{L}_C (ours)		80.1	77.0	76.3	63.3	75.9	10.4
nf2vec		—	—	—	—	—	—
Cardace et al.		—	—	—	—	—	—
\mathcal{L}_R (ours)	TRI	32.6	32.0	92.0	89.1	37.5	56.0
\mathcal{L}_{R+C} (ours)		58.7	54.4	89.6	85.2	61.7	15.0
\mathcal{L}_C (ours)		76.2	70.9	80.6	74.7	74.1	11.1

Table 3. NeRF classification of unseen architectures (multi-architecture). The encoder is trained on BOTH; the classifier is trained on the datasets in column 2 and tested on those in columns 3–8, containing NeRF architectures unseen at training time.

shown in Figure 3 (left) and discussed in Section 4.1. This trend can also be observed, as expected, when \mathcal{C} is trained on either MLP or TRI and tested on that same dataset, as this scenario replicates the previous one with smaller datasets: as shown by Figure 3 (left), \mathcal{L}_R achieves the best separation between classes of NeRFs parametrized by the same architecture. On the other hand, the introduction of a contrastive objective in the loss (i.e. \mathcal{L}_{R+C} and \mathcal{L}_C) is key to performance whenever \mathcal{C} is trained on a single-architecture dataset (e.g. TRI) and tested on another including different architectures (e.g. MLP or BOTH), as clusters of objects belonging to the same class but parameterized by different NeRF architectures are closer in the embedding space than with \mathcal{L}_R alone. In particular, \mathcal{L}_C provides the best accuracy whenever the classifier training and test sets feature different architectures (TRI vs MLP, MLP vs TRI). Overall, we achieve remarkable accuracies, both in the easier case of test sets whose architectures are part of the training set of \mathcal{C} and in the more challenging case of generalizing \mathcal{C} across architectures, a result which validates the effectiveness of the proposed architecture-agnostic representation learning framework. As shown in Table 2, in the single-architecture setting, i.e. when both the encoder and the classifier are trained and tested on either MLP or TRI, our method outperforms both nf2vec and Cardace et al.. Hence, beyond its original aim, it also turns out to be a competitive alternative to realize a single-architecture framework.

Unseen architectures. To further assess the ability of our framework to perform tasks on arbitrary NeRF architectures, we create additional test sets of NeRFs featuring architectures different than those in MLP and TRI: (i) MLP-2L, i.e. MLP where MLPs have 2 hidden layers instead of 3; (ii) MLP-32H, i.e. MLP where MLPs have hidden dimension 32 instead of 64; (iii) TRI-2L, i.e. TRI where MLPs have 2 hidden layers instead of 3; (iv) TRI-32H, i.e. TRI where MLPs have hidden dimension 32 instead of 64; (v) TRI-16W, i.e. TRI where tri-planes have spatial

Method	Encoder Training Set	Accuracy (%) \uparrow					
		MLP-2L	MLP-32H	TRI-2L	TRI-32H	TRI-16W	TRI-8C
nf2vec		63.7	—	—	—	—	—
Cardace et al.	MLP	—	—	—	—	—	—
\mathcal{L}_R (ours)		91.8	83.7	10.9	6.1	7.0	4.9
nf2vec		—	—	—	—	—	—
Cardace et al.	TRI	—	—	93.5	92.0	—	68.6
\mathcal{L}_R (ours)		10.1	10.0	92.6	82.5	22.9	72.8

Table 4. NeRF classification of unseen architectures (single-architecture). The classifier is trained on the same dataset as the encoder and tested on the datasets in columns 3–8, containing NeRF architectures unseen at training time.

resolution 16×16 instead of 32×32 ; (vi) TRI-8C, i.e. TRI where tri-planes have 8 channels instead of 16. We then evaluate our method on these new test sets without changing the previous multi and single-architecture settings, which implies that neither the encoder nor the classifier sees these architectures at training time. Multi-architecture classification results are shown in Table 3. Remarkably, a trend coherent to that of Table 1 can be noticed, namely \mathcal{L}_R tends to perform best or close to best when the classifier \mathcal{C} is trained either on BOTH or on an architecture similar to the unseen one presented at test time (e.g. trained on MLP and tested on MLP-2L or trained on TRI and tested on TRI-2L), whereas \mathcal{L}_C tends to prevail when changing the architecture type. A notable exception is TRI-16W, where the contrastive loss consistently yields the best results. Some other interesting patterns can be noted: reducing the number of hidden layers of an MLP has less impact on accuracy than reducing the hidden dimension of layers, both for the MLP-only case and when the MLP is part of a tri-plane; changing hyperparameters of tri-planes is the most disruptive change, especially if the number of channels is reduced. These patterns can be the basis of future investigation into this topic. Overall, our framework trained on BOTH proves to be quite robust and provides the first working solution to the problem of embedding NeRFs with unseen architectures. In the single-architecture setting, shown in Table 4, \mathcal{L}_R performs much better than nf2vec in the only case in which it can be tested. Instead, \mathcal{L}_R performs worse than Cardace et al. in TRI-2L and TRI-32H, i.e. TRI versions that change the MLP architecture. This is due to the fact that, when performing classification, Cardace et al. processes the tri-plane alone and discards the MLP, which makes their approach invariant to changes in the MLP architecture. Yet, since their method is tied to the tri-plane quantization, it cannot process TRI-16W and is less robust to the reduction in the number of channels. t-SNE visualizations of seen and unseen MLPs are provided in Appendix B.

4.3. NeRF Retrieval

The embeddings produced by the trained encoder can also be used to perform retrieval tasks via k -nearest neighbor

Method	Query	Gallery	Recall@k (%) \uparrow		
			k = 1	k = 5	k = 10
nf2vec (Zama Ramirez et al., 2024)			—	—	—
Cardace et al., 2024			—	—	—
\mathcal{L}_R (ours)	BOTH	BOTH	0.0	0.0	0.0
\mathcal{L}_{R+C} (ours)			11.2	32.6	46.3
\mathcal{L}_C (ours)			29.0	57.8	70.7
nf2vec (Zama Ramirez et al., 2024)			—	—	—
Cardace et al., 2024			—	—	—
\mathcal{L}_R (ours)	MLP	TRI	1.2	4.1	6.6
\mathcal{L}_{R+C} (ours)			41.2	70.2	80.9
\mathcal{L}_C (ours)			45.5	74.9	85.2
nf2vec (Zama Ramirez et al., 2024)			—	—	—
Cardace et al., 2024			—	—	—
\mathcal{L}_R (ours)	TRI	MLP	2.7	8.4	12.4
\mathcal{L}_{R+C} (ours)			42.2	69.6	79.7
\mathcal{L}_C (ours)			44.1	75.2	85.1

Table 5. **Instance-level NeRF retrieval.** The encoder is trained on BOTH. Query and gallery belong to their corresponding test sets. k -NN is computed with cosine distances.

search, as outlined in Figure 1. In particular, we define *instance-level* retrieval as follows: given a NeRF embedding of a given object (a.k.a. the *query*) and a *gallery* of NeRF embeddings, the goal is to find the embedding in the gallery that represents the same object as the query but encodes a different NeRF architecture. Naturally, this task can only exist in the multi-architecture setting, as there need to be (at least) two instances of the same object, and cannot thus be performed by either nf2vec or Cardace et al., 2024. We evaluate the performance on this task with the recall@k metric (Wang et al., 2017), defined in this context as the percentage of queries whose k nearest neighbors contain the NeRF representing the same object as the query. In Appendix A, we also show results of *class-level* NeRF retrieval, which confirm the trend observed in the classification results of Section 4.2, i.e. that the task benefits from the presence of a contrastive objective whenever the dataset on which it is performed requires reasoning across architectures (e.g. MLP query and TRI gallery). Table 5 shows the instance-level NeRF retrieval results. It is immediately clear that, when query and gallery belong to BOTH, \mathcal{L}_R is unable to perform the task: the latent space organization shown in Figure 3 (left) and discussed in Section 4.1 prevents \mathcal{L}_R from being capable of recognizing the same object represented by different NeRF architectures. \mathcal{L}_R 's performance when the (query, gallery) pair is (MLP, TRI) or (TRI, MLP) is slightly better (as the gallery is more constrained and the chance of missing the target instance is thus lower), but still very poor nonetheless. On the other hand, this is the task where the contribution of the contrastive loss emerges the most, which confirms our intuition that \mathcal{L}_C favors an architecture-agnostic latent space, as discussed in Section 4.1. \mathcal{L}_C outperforms \mathcal{L}_R in all scenarios, with \mathcal{L}_{R+C} being somewhat in the middle for (BOTH, BOTH) while being closer to \mathcal{L}_C for (MLP, TRI) and (TRI, MLP). Figure 4 displays qualitatively that the organization of the latent space captures the NeRF similarity in color and shape.

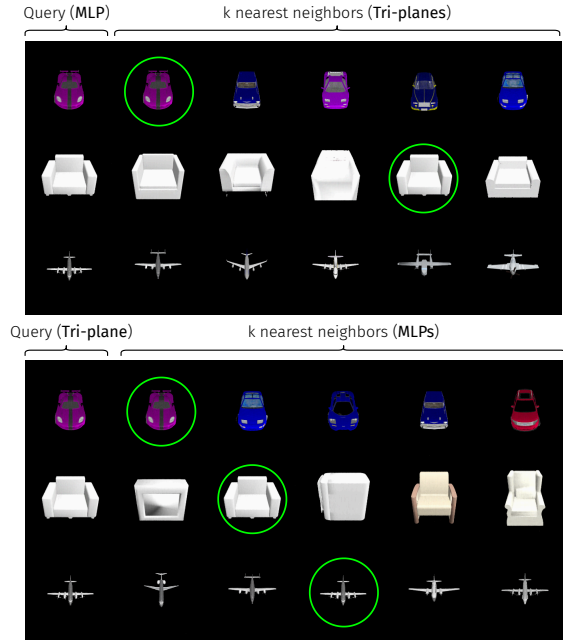


Figure 4. **NeRF retrieval (\mathcal{L}_C qualitative results).** Green circles denote NeRFs representing the same object as the query, but with a different architecture, i.e. cases in which the instance-level retrieval goal has been accomplished (for $k = 5$). Notice a failure case on the third row of the top figure. See Appendix C for an extended version of this figure.

5. Conclusions and Future Work

In this paper, we explored the task of creating a representation learning framework that directly processes NeRF weights. Our framework, based on a Graph Meta-Network encoder ingesting the NeRF parameter graph, is able, for the first time, to (i) handle any input neural architecture and (ii) process architectures unseen at training time. We investigated a rendering and a contrastive loss to train it and showed that they serve complementary purposes, favoring either class-level separability or invariance to the NeRF architecture. When tested on NeRFs implemented as MLP and tri-planes, our framework delivers excellent performance for the multi-architecture setting, and it is as effective as or better than previous methods when trained and tested on a specific NeRF architecture. The main limitation of our study lies in its experimental validation, currently limited to the two NeRF architectures considered in previous work (Zama Ramirez et al., 2024; Cardace et al., 2024), which, however, are not state-of-the-art. Verifying its effectiveness on architectures based on hash tables (Müller et al., 2022; Barron et al., 2023) that are routinely used by practitioners would enhance its practical usefulness and adoption. Finally, future work should also explore language-related tasks for NeRFs, such as the creation of NeRF assistants (Amaduzzi et al., 2024) that are architecture-agnostic.

References

- Ainsworth, S., Hayase, J., and Srinivasa, S. Git re-basin: Merging models modulo permutation symmetries. In *The Eleventh International Conference on Learning Representations*, 2023.
- Amaduzzi, A., Zama Ramirez, P., Lisanti, G., Salti, S., and Di Stefano, L. LLaNA: Large language and NeRF assistant. In *The Thirty-eighth Annual Conference on Neural Information Processing Systems*, 2024.
- Ballerini, F., Zama Ramirez, P., Mirabella, R., Salti, S., and Di Stefano, L. Connecting NeRFs, images, and text. In *Proceedings of the IEEE/CVF Conference on Computer Vision and Pattern Recognition*, pp. 866–876, 2024.
- Barron, J. T., Mildenhall, B., Verbin, D., Srinivasan, P. P., and Hedman, P. Zip-NeRF: Anti-aliased grid-based neural radiance fields. In *Proceedings of the IEEE/CVF International Conference on Computer Vision*, pp. 19697–19705, 2023.
- Battaglia, P. W., Hamrick, J. B., Bapst, V., Sanchez-Gonzalez, A., Zambaldi, V., Malinowski, M., Tacchetti, A., Raposo, D., Santoro, A., Faulkner, R., et al. Relational inductive biases, deep learning, and graph networks. *arXiv preprint arXiv:1806.01261*, 2018.
- Cardace, A., Zama Ramirez, P., Ballerini, F., Zhou, A., Salti, S., and Di Stefano, L. Neural processing of tri-plane hybrid neural fields. In *The Twelfth International Conference on Learning Representations*, 2024.
- Chan, E. R., Lin, C. Z., Chan, M. A., Nagano, K., Pan, B., De Mello, S., Gallo, O., Guibas, L. J., Tremblay, J., Khamis, S., et al. Efficient geometry-aware 3d generative adversarial networks. In *Proceedings of the IEEE/CVF conference on computer vision and pattern recognition*, pp. 16123–16133, 2022.
- Chang, A. X., Funkhouser, T. A., Guibas, L. J., Hanrahan, P., Huang, Q., Li, Z., Savarese, S., Savva, M., Song, S., Su, H., Xiao, J., Yi, L., and Yu, F. Shapenet: An information-rich 3d model repository. *CoRR*, abs/1512.03012, 2015.
- Chen, T., Kornblith, S., Norouzi, M., and Hinton, G. A simple framework for contrastive learning of visual representations. In *International conference on machine learning*, pp. 1597–1607. PMLR, 2020.
- De Luigi, L., Bolognini, D., Domeniconi, F., De Gregorio, D., Poggi, M., and Di Stefano, L. ScanNeRF: a scalable benchmark for neural radiance fields. In *Proceedings of the IEEE/CVF Winter Conference on Applications of Computer Vision*, pp. 816–825, 2023.
- Entezari, R., Sedghi, H., Saukh, O., and Neyshabur, B. The role of permutation invariance in linear mode connectivity of neural networks. In *International Conference on Learning Representations*, 2022.
- Girshick, R. Fast R-CNN. In *2015 IEEE International Conference on Computer Vision (ICCV)*, pp. 1440–1448, 2015.
- He, K., Fan, H., Wu, Y., Xie, S., and Girshick, R. Momentum contrast for unsupervised visual representation learning. In *Proceedings of the IEEE/CVF conference on computer vision and pattern recognition*, pp. 9729–9738, 2020.
- Hecht-Nielsen, R. On the algebraic structure of feedforward network weight spaces. In *Advanced Neural Computers*, pp. 129–135. Elsevier, 1990.
- Hu, B., Huang, J., Liu, Y., Tai, Y.-W., and Tang, C.-K. NeRF-RPN: A general framework for object detection in nerfs. In *Proceedings of the IEEE/CVF Conference on Computer Vision and Pattern Recognition*, pp. 23528–23538, 2023.
- Kofinas, M., Knyazev, B., Zhang, Y., Chen, Y., Burghouts, G. J., Gavves, E., Snoek, C. G. M., and Zhang, D. W. Graph neural networks for learning equivariant representations of neural networks. In *The Twelfth International Conference on Learning Representations*, 2024.
- Lim, D., Maron, H., Law, M. T., Lorraine, J., and Lucas, J. Graph metanetworks for processing diverse neural architectures. In *The Twelfth International Conference on Learning Representations*, 2024.
- Liu, L., Gu, J., Zaw Lin, K., Chua, T.-S., and Theobalt, C. Neural sparse voxel fields. *Advances in Neural Information Processing Systems*, 33:15651–15663, 2020.
- Loshchilov, I. and Hutter, F. Decoupled weight decay regularization. In *International Conference on Learning Representations*, 2019.
- Mildenhall, B., Srinivasan, P. P., Tancik, M., Barron, J. T., Ramamoorthi, R., and Ng, R. NeRF: Representing scenes as neural radiance fields for view synthesis. In *European Conference on Computer Vision*, pp. 405–421, 2020.
- Müller, T., Evans, A., Schied, C., and Keller, A. Instant neural graphics primitives with a multiresolution hash encoding. *ACM transactions on graphics (TOG)*, 41(4): 1–15, 2022.
- Navon, A., Shamsian, A., Achituv, I., Fetaya, E., Chechik, G., and Maron, H. Equivariant architectures for learning in deep weight spaces. In *International Conference on Machine Learning*, pp. 25790–25816. PMLR, 2023.

- Park, J. J., Florence, P., Straub, J., Newcombe, R., and Lovegrove, S. DeepSDF: Learning continuous signed distance functions for shape representation. In *Proceedings of the IEEE/CVF conference on computer vision and pattern recognition*, pp. 165–174, 2019.
- Radford, A., Kim, J. W., Hallacy, C., Ramesh, A., Goh, G., Agarwal, S., Sastry, G., Askell, A., Mishkin, P., Clark, J., et al. Learning transferable visual models from natural language supervision. In *International conference on machine learning*, pp. 8748–8763. PMLR, 2021.
- Sitzmann, V., Martel, J., Bergman, A., Lindell, D., and Wetzstein, G. Implicit neural representations with periodic activation functions. *Advances in neural information processing systems*, 33:7462–7473, 2020.
- Smith, L. N. and Topin, N. Super-convergence: very fast training of neural networks using large learning rates. In Pham, T. (ed.), *Artificial Intelligence and Machine Learning for Multi-Domain Operations Applications*, volume 11006, pp. 1100612. International Society for Optics and Photonics, SPIE, 2019.
- Van der Maaten, L. and Hinton, G. Visualizing data using t-SNE. *Journal of Machine Learning Research*, 9(86): 2579–2605, 2008.
- Wang, J., Zhou, F., Wen, S., Liu, X., and Lin, Y. Deep metric learning with angular loss. In *Proceedings of the IEEE international conference on computer vision*, pp. 2593–2601, 2017.
- Xie, Y., Takikawa, T., Saito, S., Litany, O., Yan, S., Khan, N., Tombari, F., Tompkin, J., Sitzmann, V., and Sridhar, S. Neural fields in visual computing and beyond. In *Computer Graphics Forum*, volume 41, pp. 641–676. Wiley Online Library, 2022.
- Xu, Q., Wang, W., Ceylan, D., Mech, R., and Neumann, U. DISN: Deep implicit surface network for high-quality single-view 3d reconstruction. *Advances in neural information processing systems*, 32, 2019.
- Zama Ramirez, P., De Luigi, L., Sirocchi, D., Cardace, A., Spezialetti, R., Ballerini, F., Salti, S., and Di Stefano, L. Deep learning on object-centric 3D neural fields. *IEEE Transactions on Pattern Analysis and Machine Intelligence*, 2024.
- Zhai, X., Mustafa, B., Kolesnikov, A., and Beyer, L. Sigmoid loss for language image pre-training. In *Proceedings of the IEEE/CVF International Conference on Computer Vision*, pp. 11975–11986, 2023.
- Zhou, A., Yang, K., Burns, K., Cardace, A., Jiang, Y., Sokota, S., Kolter, J. Z., and Finn, C. Permutation equivariant neural functionals. In *Thirty-seventh Conference on Neural Information Processing Systems*, 2023a.
- Zhou, A., Yang, K., Jiang, Y., Burns, K., Xu, W., Sokota, S., Kolter, J. Z., and Finn, C. Neural functional transformers. In *Thirty-seventh Conference on Neural Information Processing Systems*, 2023b.

In this appendix, we discuss additional experiments and provide a detailed overview of the datasets and the architecture of our method.

A. Class-level NeRF Retrieval

Class-level NeRF retrieval results in the multi-architecture setting are shown in Table 6. Following the definition by Wang et al., 2017, we call $class\ recall@k$ the percentage of queries whose k nearest neighbors contain at least one gallery element with the same class as the query. Table 6 shows that different combinations of query and gallery lead to analogous results to those observed in Table 1 for different classifier training and test sets: contrastive variants \mathcal{L}_{R+C} and \mathcal{L}_C largely outperform \mathcal{L}_R whenever query and gallery belong to different architectures, i.e. when the (query, gallery) pair is either (MLP, TRI) or (TRI, MLP), due to the organization of the latent space they induce (Figure 3). In the (BOTH, BOTH) case, on the other hand, results are comparable across models, with a larger gap only for \mathcal{L}_R at $k = 1$. This is also consistent with previous results, where \mathcal{L}_R was shown to perform the best when the classifier is tested on BOTH (Table 1).

Method	Query	Gallery	Class Recall@ k (%) \uparrow		
			$k = 1$	$k = 5$	$k = 10$
nf2vec (Zama Ramirez et al., 2024)			—	—	—
Cardace et al., 2024			—	—	—
\mathcal{L}_R (ours)	BOTH	BOTH	85.0	95.6	97.5
\mathcal{L}_{R+C} (ours)			82.5	96.2	98.2
\mathcal{L}_C (ours)			82.7	96.5	98.5
nf2vec (Zama Ramirez et al., 2024)			—	—	—
Cardace et al., 2024			—	—	—
\mathcal{L}_R (ours)	MLP	TRI	42.7	77.6	87.3
\mathcal{L}_{R+C} (ours)			86.3	98.4	99.3
\mathcal{L}_C (ours)			85.3	98.0	99.3
nf2vec (Zama Ramirez et al., 2024)			—	—	—
Cardace et al., 2024			—	—	—
\mathcal{L}_R (ours)	TRI	MLP	54.0	79.1	86.8
\mathcal{L}_{R+C} (ours)			87.1	97.5	98.9
\mathcal{L}_C (ours)			83.8	97.6	99.1

Table 6. **Class-level NeRF retrieval (multi-architecture)**. The encoder is trained on BOTH. Query and gallery belong to their corresponding test sets. k -NN is computed with cosine distances.

B. Additional Experimental Details

NeRF datasets. As described in Section 4, the MLP and TRI datasets used throughout our experimental evaluation are the NeRF datasets proposed by Zama Ramirez et al., 2024 and Cardace et al., 2024, respectively. They both train their NeRFs on ShapenetRender (Xu et al., 2019), a dataset featuring RGB images and class labels of synthetic objects belonging to 13 classes of the ShapeNetCore dataset (Chang et al., 2015): *airplane*, *bench*, *cabinet*, *car*, *chair*, *display*, *lamp*, *speaker*, *rifle*, *sofa*, *table*, *phone*, and *watercraft*. For each object, the dataset contains 36 224×224 images. We follow Zama Ramirez et al.’s train-val-test split without augmentations, consisting of 31744 NeRFs used for training, 3961 for validation, and 3961 for testing. The difference between Zama Ramirez et al., 2024 and Cardace et al., 2024 lies in the NeRF architecture they use. Zama Ramirez et al.’s are MLPs with 3 hidden layers of equal dimension 64 intertwined with ReLU activations. The input coordinates (x, y, z) are mapped to a vector of size 144 through a frequency encoding (Mildenhall et al., 2020) before being fed to the input layer of the MLP, whose outputs are the four (r, g, b, σ) predicted radiance field values. No viewing direction (θ, ϕ) is used. Cardace et al.’s NeRFs are instead made of a tri-plane with spatial resolution 32×32 and 16 channels followed by an MLP with 3 hidden layers of equal size 64 intertwined with sine activation functions (Sitzmann et al., 2020). The input coordinates (x, y, z) are mapped to a vector of size 288 through a frequency encoding before being concatenated with the tri-plane output, resulting in a vector of size $288 + 16 = 304$ being fed to the input layer of the MLP, whose outputs are the four (r, g, b, σ) predicted radiance field values. Again, no viewing direction (θ, ϕ) is used. For our datasets of unseen architectures described in Section 4.2, we follow Zama Ramirez et al.’s formulation for MLP-2L and MLP-32H and Cardace et al.’s formulation for TRI-2L, TRI-32H, TRI-16W, and TRI-8C, except for the specific architectural choice that makes each dataset different from the training ones (e.g. 2 hidden layers instead of 3 in MLP-2L).

Encoder architecture. Our framework’s encoder is a slight re-adaptation of the graph meta-network used in (Lim et al., 2024) in their experiment called *predicting accuracy for varying architectures*. It has the same network hyper-parameters: hidden dimension 128, 4 layers, a pre-encoder, 2 readout layers, and uses directed edges. However, differently from Lim et al., 2024, before average-pooling the edge features, it maps them to vectors of size 1024 through a single linear layer, resulting in a final embedding of size 1024 as in `nf2vec` (Zama Ramirez et al., 2024).

Decoder architecture. We use the `nf2vec` decoder in its original formulation (Zama Ramirez et al., 2024). The input coordinates (x, y, z) are mapped to a vector of size 144 through a frequency encoding (Mildenhall et al., 2020) and concatenated with the 1024-dimensional embedding produced by the encoder. The resulting vector of size 1168 becomes the input of the decoder, which consists of 4 hidden layers with dimension 1024 intertwined with ReLU activations, with a skip connection that maps the input vector to a vector of size 1024 via a single linear layer + ReLU and sums it to the output of the second hidden layer. Finally, the decoder outputs the four (r, g, b, σ) predicted radiance field values.

Training. Our encoder-decoder framework is trained end-to-end for 250 epochs with batch size 8, AdamW optimizer (Loshchilov & Hutter, 2019), one-cycle learning rate scheduler (Smith & Topin, 2019), maximum learning rate $1e-4$ and weight decay $1e-2$. These training hyper-parameters are the same for \mathcal{L}_R , \mathcal{L}_{R+C} , and \mathcal{L}_C . In Equation (1), foreground and background pixels are weighted by 0.8 and 0.2, respectively, as done in Zama Ramirez et al., 2024. In Equation (3), t and b are initialized to 10 and -10 , respectively, as done in Zhai et al., 2023. In Equation (4), λ is set to $2e-2$, as we experimentally observed that this choice leads to \mathcal{L}_R and \mathcal{L}_C values of the same order of magnitude.

Classification. In our classification experiments of Section 4.2, the classifier is a concatenation of 3 (linear \rightarrow batch-norm \rightarrow ReLU \rightarrow dropout) blocks, where the hidden dimension of the linear layers are 1024, 512, and 256, respectively, and a final linear layer at the end computes the class logits. The classifier is trained via the cross-entropy loss for 150 epochs with batch size 256, AdamW optimizer, one-cycle learning rate scheduler, maximum learning rate $1e-4$, and weight decay $1e-2$. These same network and training hyper-parameters are used in the classification experiments of Zama Ramirez et al., 2024.

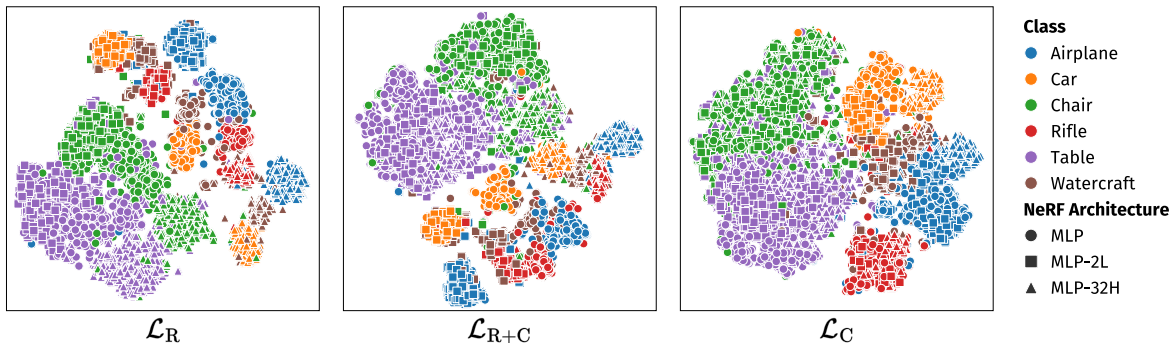


Figure 5. t-SNE plots (MLP vs unseen MLPs). Models are trained on BOTH. Classes refer to ShapenetRender objects (Xu et al., 2019).

C. Additional Qualitative Results

t-SNE. Figure 5 shows a t-SNE plot (Van der Maaten & Hinton, 2008) that, differently from the one in Figure 3, features MLPs together with the unseen MLP variants. Two remarkable conclusions can be drawn: (i) \mathcal{L}_R creates architecture-based sub-clusters for each class, not only for known architectures but also for those that it has not seen at training time; (ii) the contrastive objective pushes NeRFs of the same class with different MLP architectures closer to each other in the embedding space, although it has not been explicitly instructed to do so, as two of those architectures have not been seen at training time. This suggests that the contrastive models (especially \mathcal{L}_C) have effectively generalized the notion of similarity between underlying object appearances of different NeRF parameterizations beyond the MLP and tri-plane architectures they have been trained on.

Retrieval. Figure 6 extends Figure 4 by showing additional qualitative retrieval results. It is worth noting that, although the 44–45% recall@1 in Table 5 might suggest an undesirable outcome, by looking at all 10 nearest neighbors, one can appreciate the similarity in color and/or appearance compared to the query (e.g. similarly shaped white chairs, similar grey-colored planes, similar L-shaped sofas, and similarly rounded tables), even when the target is not among the first few neighbors. Our framework seems to have encoded both relevant information about the object’s appearance and some

invariance to the NeRF architecture that parameterizes it; nonetheless, the task of instance-level retrieval is challenging and far from being solved.

D. Implementation and Hardware

Our framework implementation is built upon the codebases by Zama Ramirez et al., 2024 (for decoder and training) and Lim et al., 2024 (for the GMN architecture and graph conversion). We plan to publicly release our code upon paper acceptance. All our experiments were performed on a single NVIDIA GeForce RTX 3090 GPU. Training either \mathcal{L}_R or \mathcal{L}_{R+C} took ~ 2 weeks, whereas training \mathcal{L}_C took ~ 4 days.

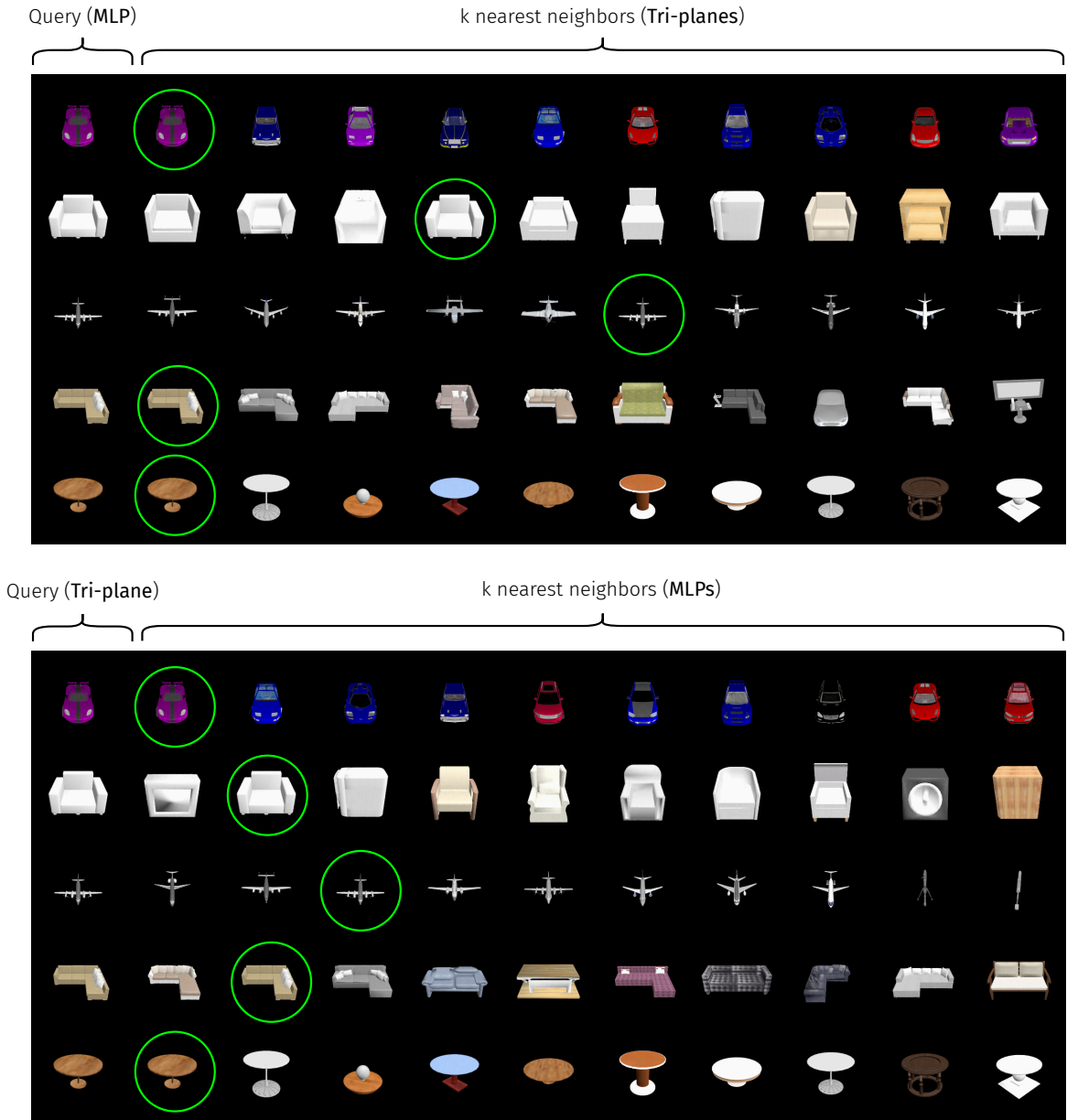


Figure 6. **NeRF retrieval (\mathcal{L}_C qualitative results)**. Extended version of Figure 4. Green circles denote NeRFs representing the same object as the query, but with a different architecture, i.e. cases in which the instance-level retrieval goal has been accomplished (for $k = 10$).